International Journal of Biological Macromolecules 196 (2022) 107–119

Contents lists available at ScienceDirect

International Journal of Biological Macromolecules

journal homepage: www.elsevier.com/locate/ijbiomac

The combined effect of thermal-acid hydrolysis, periodate oxidation, and iodine species removal on the properties of native tapioca (*Manihot esculenta* Crantz) starch

Peter N. Kariuki [a,d], Yasothai Arjunan [c], Usharani Nagarajan [b], Swarna V. Kanth [a,b,*]

[a] Department of Leather Technology, Housed at CSIR-Central Leather Research Institute, Alagappa College of Technology, Anna University, Chennai 600025, India
[b] Centre for Human & Organizational Resources Development (CHORD), CSIR-Central Leather Research Institute, Adyar, Chennai 600020, India
[c] Department of Chemistry, College of Engineering, Anna University, Chennai 600025, India
[d] Department of Chemistry, School of Science, Dedan Kimathi University of Technology, Private Bag - 10143, Dedan Kimathi, Nyeri, Kenya

ARTICLE INFO

Keywords:
Native tapioca starch
Thermal-acid hydrolysis
Periodate oxidation
Iodine species
Dialdehyde tapioca starch
ArgusLab (4.0.1)

ABSTRACT

Through a four-step top-down approach, native tapioca starch (NTS) was thermally acid-hydrolyzed, periodate-oxidized with subsequent removal of iodine species (*i.e.,* $IO_4(-)$, $IO_3(-)$, $I(-)$, and I_2), and dialdehyde tapioca starch (DTS) alcohol-precipitation. The percent yield was ~91%. Analyses confirmed the presence of aldehydic functionalities (~71%), effectual iodine species removal (~98%), and enhanced water-solubility (~96.57%). Besides, the combined treatment significantly reduced the M_w (~57.81 kDa) and ameliorated homogeneity as well as thermal stability (T_{max} ~ 667.15 °C). Structural-spectral characterization also confirmed the presence of aldehydic functionality, polymorphic transition (C- to A-type), and a higher degree of crystallinity (~91.77%), the latter further corroborated by thermal analysis. The morphological study revealed that the combined treatment reduced size (~393.55-nm-diameter and ~5.22-μm-length) and changed shape into rod-like crystals. DTS showed considerably and significantly low cytotoxicity to HaCaT cells *in vitro* at the concentrations assayed over the test period (24 h). DTS's conformation was most stable at −289 kcal/mol and −151.7 au heat formation and minimum potential energies, respectively. Overall, these results demonstrated that the combined treatment had no deleterious effects on NTS's properties, thus yielded DTS with ideal properties for multifarious uses.

1. Introduction

Tapioca (*Manihot esculenta* Crantz) is also known variously as yucca, manioc, mandioca, cassada, or cassava [1]. It is the second-largest source of starch after maize and the most-traded internationally [2]. Native tapioca starch (NTS) is extracted from tapioca tuberous roots. NTS granules are made up of two glucose polymers - amylose, a linear poly-α-1,4-D-glucan (M_w ~ 10^{5-6} Da) and amylopectin, a poly-α-1,4-D-glucan branched by α-1,6-D-glucan (M_w ~ 10^{7-8} Da), with the latter (*i.e.,* amylopectin) constituting the largest proportion [3]. Dry NTS is a white, odorless, tasteless, and insoluble powder, and the aqueous suspension is neutral to litmus [4]. Besides, the paste has high clarity and tackiness [5]. These attributes allow its direct use in a wide range of food and industrial products as an adhesive, colloidal/emulsion stabilizer, thickener, and bulking, gelling, and water retention agent [6]. Native starches, however, possess several innate weaknesses, which limit their application, *e.g.*, syneresis, retrogradation, textural change, low water holding capacity, and thermal and shear resistance. These drawbacks can be overcome by appropriate physical, chemical, or enzymatic treatment processes while considering the intended use of the end-product [5]. And so, with reference to NTS combined treatment, four processes were employed, as follows: 1) thermal-acid hydrolysis - to enhance NTS water-solubility; 2) periodate oxidation - to introduce aldehydic functionalities; 3) iodine species removal - to avert physico-chemical property changes, especially color pre- and post-application; and 4) alcohol-precipitation - to isolate DTS. The first three treatment processes are concisely and lucidly discussed.

Thermal-acid treatment of starch combines the two most common pre-treatments: hydro-thermal treatment and acid hydrolysis [7]. Exploring the individual effect of each process is important for understanding heat and acid action on starch granules. Therefore, hydro-thermal treatment results in starch gelatinization, a topic that has

* Corresponding author at: CHORD - CSIR-Central Leather Research Institute, Adyar, Chennai 600020, India.
E-mail address: swarna@clri.res.in (S.V. Kanth).

https://doi.org/10.1016/j.ijbiomac.2021.11.211
Received 2 August 2021; Received in revised form 8 November 2021; Accepted 30 November 2021
Available online 13 December 2021

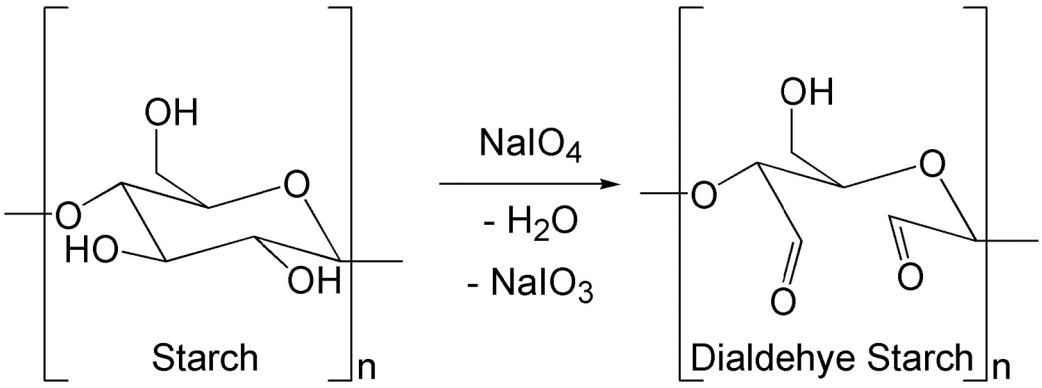

Scheme 1. Periodate oxidation of starch.

been reviewed extensively by other authors [8–11]. Briefly, the heating of aqueous starch suspension generates a fluid comprising a mixture of porous, gelatinized and swollen granules with an amylopectin skeleton in an amylose solution. On cooling, gel networks are formed, converting random amylose coils into a crystalline structure. Likewise, the mechanism and effects of acid hydrolysis on the properties of starch from various sources have been reviewed in detail previously [12–14]. Concisely, amylose and amylopectin on the granule surface are attacked simultaneously in the initial stages of acid hydrolysis. In addition, the amorphous zones composed mainly of amylopectin are predominantly hydrolyzed, increasing the relative proportion of crystalline regions.

The preparation, properties, and applications of dialdehyde starches have also been well-studied and reviewed [15–18]. Periodate oxidation exploits the three-hydroxyl groups at C-2, C-3, and C-6 of the anhydroglucose units. The reaction is characterized by the selective cleavage of the C-2–C-3 bond and concomitant conversion of the secondary hydroxyl groups at C-2 and C-3 into aldehyde moieties (-CHO), thereby causing the opening of the anhydroglucose rings, as shown in Schematic 1 (Section 3.1). The primary hydroxyl groups at C-6 are oxidized to carboxyl groups (COOH). Treatment with periodate also breaks glycosidic linkages during oxidation. Accordingly, aldehyde content significantly influences physico-chemical properties, particularly the average molecular weight, crystallinity, and hydrophilicity.

Dialdehyde starch contains iodate ($IO_3(-)$), which is a periodate ($IO_4(-)$) reduction product (Scheme 1, Section 3.1). It may also contain residual periodate and other iodine species such as iodide ($I(-)$) and molecular iodine (I_2) [19]. As earlier mentioned, iodine species removal is imperative to avoid changes in dialdehyde starch pre- and post-application. Residual periodate interferes with (or changes) the physico-chemical properties of dialdehyde starch [20]. The presence of iodate in dialdehyde starch causes a color change ascribable to $IO_3(-)$ ions reduction to I_2 molecules that yellow in low or brown and darken at higher concentrations [21]. It has also been found that iodine makes iodine-exposed (starch) granule surfaces more crowded and inhomogeneous [22]. Periodate and iodate ions may be removed as such by precipitation using inorganic salts or the use of an anion-exchange resin [23]. Dialdehyde starch - free of iodine species has a wide array of potential applications, including: 1) as a novel cross-linker for stabilizing skin/hide collagen matrix, synthetic tanning or retanning, and protein leather finishing [19,24]; 2) as a therapeutic agent substituting other aldehydes, such as formaldehyde and glutaraldehyde owing to their toxicity and usage restrictions [25]; and 3) as a new drug-carrier system in the pharmaceutical industry aiding in targeted and sustainable drug-delivery mechanisms [26].

Computation allows the integration of the experimental data obtained from different sources to substantiate the existing *in vitro* experiments. The vacuum-medium helps visualize the geometrical orientation and structural confinement of the projected models, such as NTS and DTS. Therefore, in this study, NTS is considered a collection of atoms held together by classical forces. Further, the NTS molecule is through a four-step approach treated to obtain DTS as described in the experimental section (Section 2.2). These models are subjected to force field projections to calculate the potential energy function by summing a set of energy functions and the corresponding parameters, *viz.* stretching, bending, torsion, Van der Waals, electrostatic, and hydrogen bond energies and cross term. Accurate calculations are carried out based on the geometric properties of molecules, particularly dipole moments, local charges, such as zero-differential orbital (ZDO), and Mulliken atomic charges, and the bond order generated from ArgusLab (4.0.1) using the Austin Model 1 (AM1) parameterized method. ArgusLab (4.0.1) operates on quantum mechanics-based principles to predict the potential energy, geometry optimization, solvation properties, and electrostatic potential surface properties [27]. Given the above considerations, this simulation helps in substantiating the structural data obtained from wet lab calculations and portrays the visual processing of the molecular orbital arrangement.

Each of the four NTS treatment processes has distinct effects on its properties and have so far been examined and reviewed in great depth, as outlined above. There is, however, no literature on the combined effect of thermal-acid hydrolysis, periodate oxidation, and, more importantly, the removal of iodine species on NTS properties. The examining of the combined treatment effect on NTS properties is the contribution of this work. Among the four treatment processes, iodine species removal adds to and illuminates the novelty and significance of the research. Moreover, no study has been found to analyze NTS and DTS molecular conformations using ArgusLab (4.0.1). Therefore, the objectives of this study are summarized, as follows: 1) Preparation of DTS; 2) Removal of iodine species from DTS; 3) NTS and DTS chemical analyses, characterization, *in vitro* cytotoxicity (MTT) assay, and conformational analysis (geometry optimization); and 4) Detailed examination of the effect of the combined treatment on NTS properties.

2. Experimental

2.1. Materials

NTS was purchased from Angel Starch & Food Pvt. Ltd. (Tamil Nadu, India). All chemicals used were of analytical grade and were bought from Sigma-Aldrich (New Delhi, India) and Sisco Research Laboratories (SRL) Pvt. Ltd. (Mumbai, India).

2.2. DTS preparation

A four-step procedure was used. In the first step (*i.e.*, thermal-acid hydrolysis [28] - slightly modified), a 5% (*w/v*) NTS suspension was prepared at 60 °C, slightly below the gelation onset temperature (~63 °C), with constant stirring (1000 rpm, 30 min) on a magnetic stirrer (IKA® C-MAG HS4 digital, Germany). Concentrated (98%)

sulphuric acid (0.92 g H_2SO_4) was slowly added (*n.b.* drop-wise) to the suspension while stirring, and the mixture was heated at 70 °C for 2 h. The hydrolysate was then cooled to 50 °C, and the pH adjusted to *ca.* 4.5 with NaOH or H_2SO_4. A handheld pH-meter (LAQUAact-PC110; Horiba Scientific, Japan) with a LAQUA electrode was used to monitor pH throughout the experiment. In the second step (*i.e.,* periodate oxidation [29] - slightly modified), 7.43 g of sodium metaperiodate ($NaIO_4$) was added, and the pH was adjusted to ~3.75. The oxidation reaction was carried out in the dark at 50 °C for 4 h under constant stirring (500 rpm), after which the temperature was reduced to 35 °C for 44 h with regular pH monitoring. In the third step (*i.e.,* iodine species removal), periodate ($IO_4(-)$) in the aqueous solution of oxidized NTS was analyzed as reported previously by Babor et al. [30] and iodate ($IO_3(-)$) by iodometric (redox) titration [31]. The iodine species were removed by the addition of a stoichiometric quantity (~3.64 g) of sodium pyrosulphite ($Na_2S_2O_5$) to an 80 mL aliquot with vigorous stirring (~700 rpm) for 15 min at room temperature. The mixture was centrifuged at 4500 rpm for 10 min, and the supernatant was retained. Iodide ($I(-)$) was precipitated as a silver-salt at pH 7 by the addition of $AgNO_3$ (addition of $NO_3(-)$ was negligible). Excess Ag was removed as AgCl precipitate by adding HCl. The supernatant was repeatedly washed with carbon tetrachloride (CCl_4) to remove any residual molecular iodine (I_2). In the fourth step (*i.e.,* alcohol-precipitation [29] - slightly modified), DTS was precipitated from the supernatant aliquot obtained in the third step by adding 2-methylpropan-2-ol at a ratio of 1:3 (*v/v*) and filtered off. The filtrate was washed twice with double-distilled-deionized water (DDDW) to remove any excess salts by dissolving it in DDDW and alcohol-precipitating DTS, as described above. The precipitate (*i.e.,* DTS) was dehydrated with absolute ethanol, centrifuged, oven-dried at 60 °C for 6 h, packed, and stored in a desiccator containing anhydrous sodium sulfate (*n.b.* a drying agent suitable for aldehydes) until further use.

2.3. Characterization

2.3.1. Apparent amylose content (AAC)

The AAC of NTS was determined by the colorimetric iodine affinity method of Adedokun and Itiola [32].

2.3.2. Water-solubility (WS)

The WS of NTS and DTS at ambient temperature were determined following the procedures outlined by Cruz et al. [33] and Ozkan et al. [34], respectively.

2.3.3. Aldehyde content (AC)

DTS was analyzed for AC using the rapid quantitative alkali consumption method, as Hofreiter et al. [35] reported. The percentage of dialdehyde units was calculated from the following expression:

$$\mathrm{Da}\% = \frac{C_1V_1 - 2C_2V_2}{W/161 \times 1000} \times 100\%$$

where C_1 (mol/L), V_1 (mL) are the normality and the total volume of NaOH; C_2 (mol/L), V_2 (mL) are the normality and the total volume of H_2SO_4; W is the dry weight (g) of the DTS sample; and 161 is the average molecular weight of the repeat unit in DTS.

2.3.4. Gel permeation chromatography (GPC)

NTS and DTS molecular weights and molecular-weight distributions were determined using GPC equipped with a multi-angle laser-light scattering (GPC-MALLS) system (DAWN HELEOS 8+; Wyatt Technology Corporation, Santa Barbara, CA, USA) and a differential refractive index (dRI) detector (Wyatt, Optilab-rEX). Detector calibration, sample preparation, and analysis were carried out as detailed in Fiedorowicz and Para [36].

2.3.5. Powder X-ray diffractometry (PXRD)

Powder X-ray diffractograms of NTS and DTS were obtained using a Mini Flex-II Desktop X-ray diffractometer (Rigaku, Japan) with a source of Cu-Kα radiation (λ = 1.54 Å) at 30 kV, 15 mA, and ambient conditions. The scan range was 5–80° (2θ) with a scanning speed of 4°/min and a sampling interval of 0.02°. Relative crystallinity (%) of samples was quantitatively estimated in the region 2θ = 5–50° following the method of Zhang et al. [37] using OriginPro 8.5 (OriginLab, USA).

2.3.6. ^{13}C CP/MAS solid-state nuclear magnetic resonance (SS-NMR) spectroscopy

Carbon-13 cross-polarization/magic-angle spinning (^{13}C CP/MAS) SS-NMR spectra were recorded on a Bruker Avance - III HD 400 MHz Narrow-Bore FT-NMR Spectrometer (Switzerland) operating at 100.61 MHz (carbon-13) resonance frequency (RF). Experiments were conducted using a 4-mm double-resonance CP/MAS probe at a regulated temperature of 294.3 K. For analysis, the fine-powder samples (*ca.* 150 mg, dry basis) were packed and sealed in o.d. zirconia rotors under an inert atmosphere. Each spectrum was obtained at a CP contact time (τ), 90° proton pulse width, and RF field strength of 3 ms, 4 μs, and 30.0 kHz, respectively, with a recycle delay of 4 s and 164 scans [38,39].

2.3.7. Thermo-gravimetric analysis (TGA)

A TA Instruments (India) thermo-gravimetric analyzer (TGA Q50 V20.5 Build 30) was used for thermal decomposition studies. From each sample, *ca.* 10 mg (dry basis) was loaded into a platinum pan and heated under a steady flow of dry nitrogen maintained at a flow-rate of 40 mL/min from 25 to 800 °C at 10 °C/min. TG and derivative thermo-gravimetric (DTG) data were obtained for each sample [40].

2.3.8. Scanning electron microscopy (SEM)

The morphological features of samples were observed with a scanning electron microscope (Carl Zeiss MA15/EVO 18 SEM, Germany) operated at an accelerating potential of 10 kV and a working distance of 11 mm. The as-prepared dry-powder samples were mounted on a circular aluminum stub using double-sided cellophane tape and sputter-coated with a thin conductive layer of gold (~20 nm) to avoid charging under the high electron beam during micrography. Photomicrographs were taken at 2500 x and 5000 x magnification [41].

2.3.9. Color evaluation

Color measurements, *viz.* L* (darkness/lightness; ranging from L = 0 (black) to L = 100 (white)), a* (−a (greenness) to +a (redness)), b* (−b (blueness) to +b (yellowness)), and C* (chromaticity) were obtained by recording the reflectance spectra in the range 300–830 nm using a Varian Cary 5000 UV–Vis-NIR spectrophotometer (Agilent Technologies, USA) as outlined by Priya et al. [42].

2.3.10. In vitro cytotoxicity (MTT) assay

The effect of DTS on cell proliferation was evaluated *in vitro* using HaCaT cell lines as described previously in detail [43], but with slight modification. Briefly, different DTS concentrations (10, 25, 50, and 100 μg/mL) were dissolved in phosphate buffer saline (pH 7.4) and used for the assay. The solutions were added into 12-well culture plates containing Dulbecco's modified eagle medium (DMEM) supplemented with 10% fetal bovine serum and 1% antibiotic. HaCaT cells were seeded in the wells at a density of 4×10^4 cells/well and incubated in 5% CO_2 at 37 °C for 24 h. The well containing cell culture medium without a DTS sample was used as the control. Cell morphology was observed using an optical microscope and 300 μL of the yellow tetrazolium MTT (3-(4,5-dimethylthiazol-2-yl)-2,5-diphenyltetrazolium bromide) solution added to each well, followed by incubation for 4 h until a purple precipitate was visible. The absorbance of each well was recorded at 570 nm in an automatic microplate reader (Synergy H4, BioTek Co., Japan). Following that, the percent cell viability was calculated from the optical density of the sample *versus* that of the control.

$$S_2O_5^{2-}{}_{(aq)} + H_2O_{(l)} \rightleftharpoons 2HSO_3^{-}{}_{(aq)} \quad (R1)$$

$$IO_3^{-}{}_{(aq)} + 3HSO_3^{-}{}_{(aq)} \longrightarrow I^{-}{}_{(aq)} + 3H^{+}{}_{(aq)} + 3SO_4^{2-}{}_{(aq)} \quad (R2)$$

$$Ag^{+}{}_{(aq)} + I^{-}{}_{(aq)} \longrightarrow AgI_{(s)} \quad (R3)$$

$$6H^{+}{}_{(aq)} + 5I^{-}{}_{(aq)} + IO_3^{-}{}_{(aq)} \longrightarrow 3I_{2(aq)} + 3H_2O_{(l)} \quad (R4)$$

$$I_{2(s)} + CCl_{4(l)} \longrightarrow I_2(CCl_4) \quad (R5)$$

$$I_{2(s)} + HSO_3^{-}{}_{(aq)} + H_2O_{(l)} \longrightarrow 2I^{-}{}_{(aq)} + HSO_4^{-}{}_{(aq)} + 2H^{+}{}_{(aq)} \quad R6$$

Scheme 2. Iodine species removal reactions.

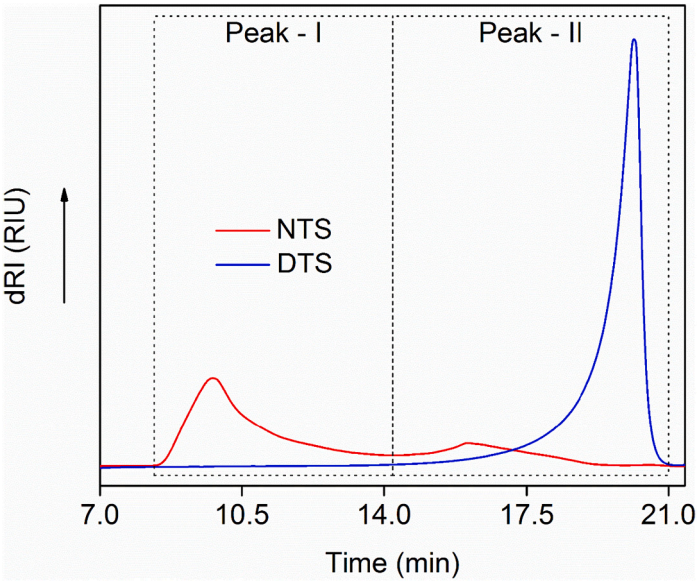

Fig. 1. DRI chromatographic profiles of NTS and DTS.

2.3.11. Computational and molecular modeling

Conformational analysis of NTS and DTS was performed on a Windows-based computer. The SMILES notation for NTS - OC2C(OC1OC(*CO*)C(O)C(*O*)C10)C(*CO*)OC(O)C20 and DTS - OC(C(*O*)OCC(C)C)C(OCCOCC(*C*)C)CO were used for structural building. The structures were generated with ACD/ChemSketch v.2020.1.1 (ACD/Labs, Toronto, ON, Canada), and structural modeling was performed using ArgusLab 4.0.1 (Mark A. Thompson, Planaria Software LLC, Seattle, WA, USA, http://www.arguslab.com), a structure-building module [44]. The built structures were subjected to energy minimization using the geometry optimization package in this module. The AM1 parameterization of the Modified-Neglect of Diatomic-Differential Overlap (MNDO) method based on a closed-shell Restricted Hartree-Fock (RHF) calculation [45] was employed. The calculations were carried out, taking into account the dipole moments, atomic charges, and surface properties.

2.3.12. Statistical analysis

The reported data were averages ± SD (standard deviation) of three independent replicate measurements. Analysis of the significant differences between sample means was carried out *via* one-way single-factor ANOVA (analysis of variance) followed by pairwise comparison using Tukey-Kramer HSD (honestly significant difference) post-hoc test at $\alpha = 0.05$. Data management and statistical calculations were conducted using EXCEL® 2016 (Microsoft Corp., USA) and OriginPro 8.5 (OriginLab, USA).

3. Results and discussion

3.1. Chemical analyses

The AAC of NTS as determined using the colorimetric iodine affinity method was found to be 28.01% (±0.16). In similar studies on NTS, Wongsagon et al. [20] and Wickramasinghe et al. [46] reported comparable AAC values of 28.50% and 28.8%, respectively. A 30% amylose value is the highest reported in cassava starch literature and could vary according to the variety [46]. Besides, normal starches contain 25–30% amylose [47].

Here, it is pertinent to underline again that the essence of thermal-acid hydrolysis was to improve water-solubility. Therefore, in one of our experiments, direct periodate oxidation and iodine species removal yielded a water-insoluble product at ambient temperature, further stressing the significance of hydrolysis prior to oxidation. The percent WS of NTS and DTS were 21.21 ± 0.05 and 96.57 ± 0.30, respectively. The results showed that DTS solubility was markedly higher than that of

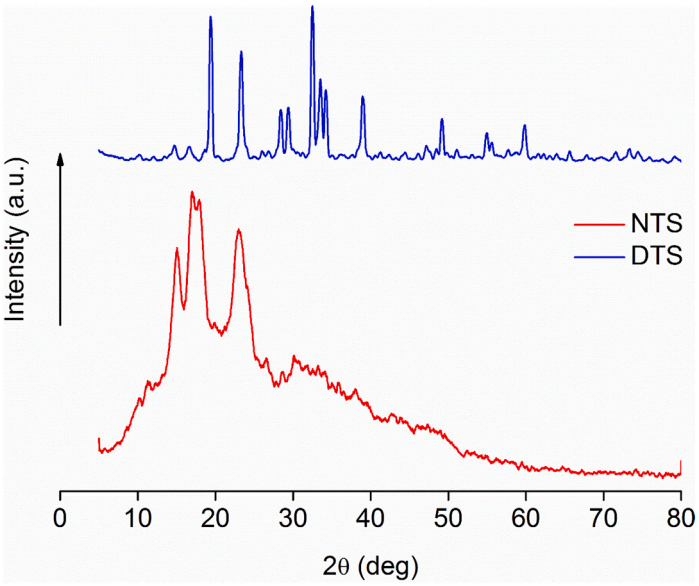

Fig. 2. X-ray powder diffraction patterns of NTS and DTS.

NTS, indicating a considerably enhanced hydrophilicity. This could be explained by the fact that thermal-acid hydrolysis and subsequent periodate oxidation of starch at low pH reduce the molecular weight and increase solubility and reactivity. Moreover, and apart from the two-aldehyde groups, dialdehyde starch possesses a hydrophilic hydroxyl group per repeating unit that enhances its water-binding ability [34,40].

At the same time, it is also necessary to accentuate that periodate oxidation offers an effective route to introduce aldehyde groups to NTS. Thus, the AC of DTS estimated using the rapid quantitative alkali consumption method was 71% and a percent yield of 91%. The aldehyde content was higher than what Wongsagon et al. [20] reported. In point of fact, ^{13}C CP/MAS SS-NMR (Fig. 3) confirmed the formation of aldehyde carbonyl groups. More importantly, the introduced aldehyde functional groups provide abundant active sites and correspondingly boost reaction activity [40].

In addition, it is germane to emphasize that the object of removing iodine species from DTS was to halt physico-chemical property changes, and particularly of color, prior to or subsequent to application. Therefore, an analysis of the aqueous solution of periodate-oxidized NTS showed no presence of $IO_4(-)$ ions. As per our experiments, a well-optimized periodate oxidation reaction should not contain residual $IO_4(-)$ as it is depleted during the reaction. In view of that, the absence of $IO_4(-)$ indicated that the periodate was entirely exhausted in the process. Iodate analysis confirmed the presence of $IO_3(-)$ ions. As already pointed out, iodate is a periodate reduction product (Scheme 1). The percentage removal of iodate was 98%. In respect to iodine species removal, Scheme 2 shows metabisulfite ($S_2O_5(2-)$) dissolves in water to form bisulfite ions ($HSO_3(-)$) (Reaction - R1), which reduce $IO_3(-)$ to I(−) (Reaction - R2) in a reaction referred to as the Landolt reaction [48]. The generated I(−) was precipitated as a silver salt (Reaction - R3). Although kinetically slow, residual $IO_3(-)$ may oxidize the generated I(−) to form I_2 (Reaction - R4) in a reaction known as the Dushman reaction [49]. Three washes with CCl_4 removed any generated I_2 (Reaction - R5). Moreover, $HSO_3(-)$ was added in excess to avoid I_2 accumulation by reducing it back to I(−) (Reaction - R6).

3.2. Molecular-weight distribution (MWD)

Bi-modal and uni-modal distributions of fractions designated peaks I and II were observed in NTS and DTS fractograms, respectively (Fig. 1). It can be seen from the NTS fractogram that amylopectin (Peak - I) eluted at 9.78 min with a weight-average molecular weight (M_w) of 22,620 kDa and a corresponding polydispersity index (PDI) of 2.37. Amylose (Peak - II) eluted at 16.01 min with a M_w of 1001 kDa and PDI of 9.77. The order of elution was, of course, explained by the fact that amylopectin is a heavily branched and high-molecular-weight component of NTS and thus eluted first, followed by the linear low-molecular-weight amylose fraction [50]. Amylose M_w (~1001 kDa) was one order lower than that of amylopectin (M_w ~ 22,620 kDa). Comparable amylopectin and amylose M_w have previously been reported [3,51]. With reference to the PDI of NTS, Peak - I (PDI ~ 2.37) had a narrow MWD pattern, while that of Peak - II (PDI ~ 9.77) was broad, indicating that amylopectin molecules were significantly more homogeneous than those of amylose were. It is noteworthy that the peak areas of amylopectin (Peak - I) and amylose (Peak - II) fractions depict the MWD. Therefore, the percentage peak areas corresponding to the eluted amylopectin and amylose fractions were 73.29% and 25.71%, respectively. Interestingly, the AAC (~28.01%) and amylose peak (Peak - II) area (~25.71%) were comparable. In addition, Peak - I to Peak - II area ratio is a measure of the extent of amylopectin branching. Thus, the calculated peak area ratio was 2.85. The higher the ratio, the greater the branching [52]. In the case of DTS, the fractogram exhibited a single dominant peak centered at 20.14 min, corresponding to a M_w, PDI, and percentage peak area of 57.81 kDa, 1.661, and 100%. A peak shift to a lower-molecular-weight region (*i.e.,* right-side) of the fractogram corresponded to an increase in retention time. The impact of the combined treatment of NTS with acid and oxidant and the subsequent removal of iodine species was apparent from the fractograms. Comparing the two fractograms revealed that the NTS amylopectin Peak - I centered at 9.78 min disappeared with the combined treatment, and the MWD changed from bi-modal to uni-modal. It appears that amylopectin was subject to more intensive hydrolytic and oxidative degradation than amylose. In a study conducted by Atichokudomchai et al. [53], it was reported that NTS hydrolysis occurred mainly in the amylopectin domains. The DTS peak was detected at a higher retention time and was narrower (PDI ~ 1.66) than those of NTS, indicating a reduction of M_w and greater homogeneity with the combined treatment. There was also an increase in DTS peak height and a sharpening of the peak into a more symmetric shape. Further, the M_w of DTS (~57.81 kDa) was three and two orders lower than that of amylopectin (M_w ~ 22,620 kDa) and amylose (M_w ~ 1001 kDa), respectively, indicating fractions of lower-molecular-weight, *viz.* depolymerized amylopectin and amylose fragments. The estimated gelatinization-viscosity of NTS (~902.56 ± 5 mPa.s) was markedly and similarly lower than that of DTS (~35.36 ± 0.4 mPa.s). The decrease in

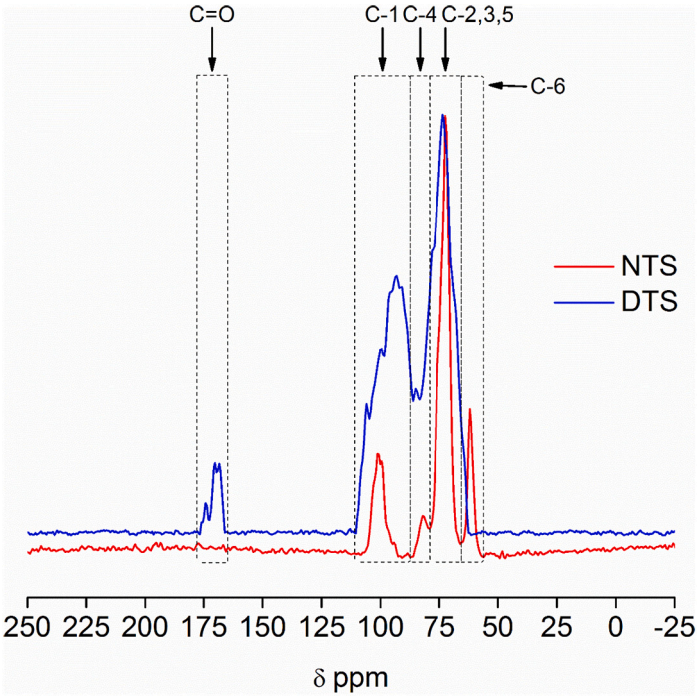

Fig. 3. ^{13}C CP/MAS SS-NMR spectra of NTS and DTS.

M_w and gelatinization-viscosity was attributed to the cleavage of NTS glycosidic linkages following its treatment with an acid and oxidant, which hydrolyze both α-(1,4)-D-glycosidic linkages and α-(1,6)-D-glycosidic inter-chain linkages [40,51]. Besides, it is plausible that the resulting DTS rod-like crystals were more homogeneous owing to iodine species removal, which was, in effect, confirmed by SEM (Fig. 5).

3.3. Structural-spectral properties

3.3.1. X-ray diffraction and crystallinity

Fig. 2 shows the PXRD spectrograms with Bragg diffraction peaks that reflect the crystalline nature of NTS and DTS. It can, therefore, be seen that NTS exhibited strong diffraction peaks at 2θ ~ 15.06°, 17.06°, 18.00°, 22.90°, and 23.00° with auxiliary peaks at 2θ ~ 11.54°, 26.60°, 30.08°, and 33.22° typifying A-type crystalline packing. B-type polymorph signature peaks occurred at 2θ ~ 5.77° and 10.24°, alongside other Bragg reflections at 2θ ~ 11.28°, 13.30°, 16.98°, 22.66°, 23.20°, 24.10°, 26.54°, and 30.68°. Moreover, the peaks at 2θ ~ 7.34°, 13.14°, and 19.92° depicted a single-helix V-type polymorph. Taken together, these results were indicative of a C-type polymorph, a combination of the double-helical A- and B-type polymorphs. The results were comparable to those reported by other authors [39,54,55]. It should be noted that the Bragg peak at 2θ ~ 23° is only present in amylopectin-rich starch [56], substantiating the high NTS amylopectin content (~71.99% (±0.16)). The effect of the combined treatment on the crystalline structure of NTS was evident from the diffractograms. NTS's prominent crystal peaks and the amorphous region on the diffractogram disappeared with the combined treatment, and the relative crystallinity increased from ~32.67% (NTS) to ~91.77% (DTS), which was further substantiated by the observed rod-like crystals in SEM (Fig. 5(B, b). The relative crystallinity of NTS corresponded well with literature values that range from 15 to 45% [57]. It has to be underlined that most starch granules consist of alternating crystalline and amorphous lamellae [58]. The amorphous regions, *viz.* linear amylose, and branching parts of amylopectin influence the diffraction intensity and relative crystallinity [40]. Interestingly, GPC results revealed that amylopectin was much more susceptible to hydrolytic and oxidative degradation than amylose was. It was also observed that the M_w decreased with a concomitant increase in relative crystallinity. This can be attributed to the degradation of the amorphous material of the NTS granules resulting in more crystals integrated with depolymerized amylose fractions [59]. Mutungi et al. [60] assert that the absence of long polymer chains that inhibit intra-polymer hydrogen bonding because of their random conformation favors recrystallization. Besides, according to Atichokudomchai et al. [53], acid hydrolysis of NTS degrades linear amylose and mainly the amorphous branching parts of amylopectin, increasing the percentage of relative crystallinity. Diffraction peaks at 2θ ~ 19.38°, 23.32°, and 33.52° and the absence of B-type polymorph distinctive Bragg peaks (*i.e.,* 2θ ~ 5.77° and 10.24°) suggested the crystalline phases observed in the DTS diffractogram were most likely A-type with V-type residues, indicating a possible transition from C- to A-type polymorph. The transition of crystallinity (*i.e.,* C to A) could be attributed to the preferential hydrolytic and oxidative degradation of B-type polymorph and a subsequent rearrangement of decoupled double helices [12]. Further, the packing of crystals in B-type is less dense than in A-type, allowing easy penetration of the acid and oxidant during degradation, which explains the preferential attack of B-type lattice sites [55]. Additionally, and importantly, the removal of iodine species could have also allowed for a much better crystal packing in consequence of the enhanced surface morphology and homogeneity, as confirmed by SEM (Fig. 5).

3.3.2. Solid-state carbon-13 NMR spectral properties

As anticipated, NTS exhibited NMR spectral features (Fig. 3), largely synonymous with those of starch in a broad region between δ 55–110 ppm [61]. Non-anomeric carbons, *viz.* C-6, C-2,3,5, and C-4 were assigned to resonance signals at δ 61.79, 72.15, and 81.94 ppm, respectively. The strongest signal was that of combined C-2,3,5 carbon atoms of the glucose unit as a single intense peak, while that of C-4 was weak and merged with the C-2,3,5 signal. As previous studies have indicated, the merging of the two signals arises from moisture present in NTS [62] and the non-crystalline part of the C-4 site [63]. Besides, the C-4 signal in hydrated samples appears downfield at between δ 80 and 82 ppm as a separate peak but merged with the C-2,3,5 signal [62]. The anomeric carbon (*i.e.,* C-1) exhibited a doublet at δ 101.00 and 99.66 ppm with a moderate shoulder at δ 94.35 (*i.e.,* bottom-right). Typically, C-1 resonance provides information on ordered crystalline and

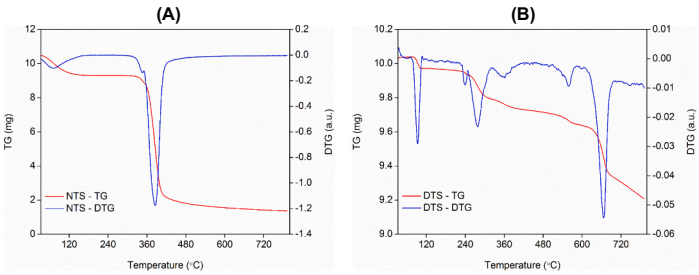

Fig. 4. TG-DTG thermal curves of NTS (A) and DTS (B).

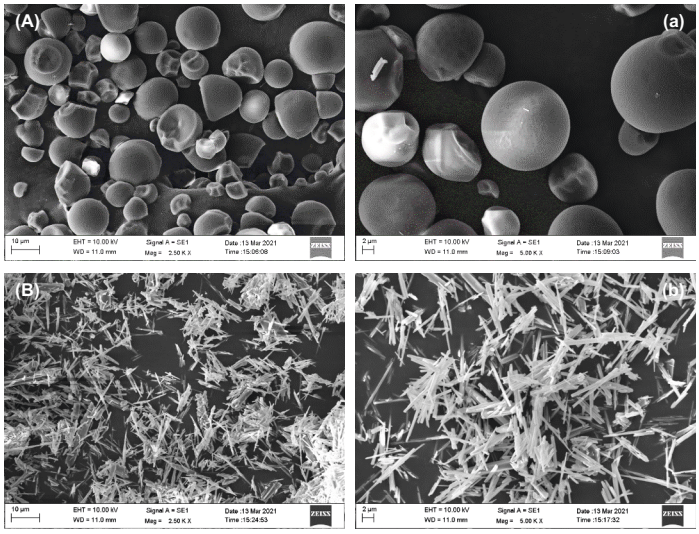

Fig. 5. NTS (A, a) and DTS (B, b) SEM photomicrographs.

Table 1
Colorimetric parameters of white standard, NTS, DAS, and DTS.

Test sample	*L**	*a**	*b**	*c**
White standard	99.995 ± 0.001[a]	0.006 ± 0.001[a]	−0.003 ± 0.001[b]	0.007 ± 0.004[b]
NTS	97.557 ± 0.003[a]	0.660 ± 0.003[a]	3.722 ± 0.005[ab]	3.780 ± 0.009[ab]
DAS	72.201 ± 0.012[a]	8.956 ± 0.014[a]	36.559 ± 0.027[a]	37.641 ± 0.038[a]
DTS	93.873 ± 0.002[a]	0.480 ± 0.006[a]	2.639 ± 0.008[b]	2.682 ± 0.016[b]

Mean ± SD (n = 3). Any two means within a column followed by a common letter superscript are not significantly different (Tukey's HSD post-hoc test; α = 0.05).

amorphous starch domains, specifically crystallinity, conformation, and the double helix symmetry. Native A- and B-type crystal lattices comprise left-handed parallel-stranded double-helical structures assembled in monoclinic and hexagonal lattices, respectively [39]. A- or B-type polymorphism can be inferred from the multiplicity of C-1 resonance. In A-type starch, the anomeric carbon signal is a triplet and a doublet for B-type polymorph [62]. Thus, the doublet appearing at δ 101.00 and 99.66 ppm in the C-1 resonance peak revealed B-type polymorphism. This finding correlated well with the PXRD results. Further, it may also be noted that C-1 resonance peaks at δ 101.00, and 99.66 ppm correspond to amylose and amylopectin non-identical sugar residues [64]. As reported previously [64], C-4 resonance is associated with single helices in amorphous zones in starch. Accordingly, the shoulder peak position, *i.e.,* δ 81.94 ppm, was in accord with the V-type polymorph C-4 chemical shift [64], which also validated results obtained by PXRD analysis. The broad peak at δ 72.15 ppm corresponds to carbons 2, 3, and 5 of the glucose units in amorphous domains [64], and the C-6 signal at δ 61.79 indicates the presence of α-1,6-glucoside bonds [65]. In their study, Khatoon et al. [61] pointed out that C-6 chemical shifts at ~60, ~62, or ~66 ppm correspond to *gg, gt,* and *tg* conformations, which suggested NTS was a *gt* conformer. It is evident from the DTS spectrum that the combined treatment caused significant and marked molecular structural changes in NTS. The anomeric carbon (C-1) intensity and peak area decreased, and the doublet transitioned to a triplet (*i.e.,* B to A) with split peaks at δ 105.84 and 97.75 ppm and the central peak at δ 93.37 ppm, which shifted upfield on account of increased electron density. This concurred well with the study findings reported by [12] and showed preferential hydrolytic and oxidative degradation of B-type polymorphs, which agreed with PXRD results. Notably, the C-4 resonance signal at δ 84.95 ppm almost disappeared with the treatment. The peak area significantly reduced and was ascribed to the C-4 amorphous domains' proneness to degradation. Unlike what was reported by Wang and Copeland [43], the resonance signal at δ 73.39 ppm showed no significant change after treatment apart from a decrease in intensity and peak area and a downfield chemical shift owing to decreased electron density. Yu et al. [66] attributed the decreased C-1 and C-4 signal intensities to the extensive degradation of α-(1–4)-glucosidic linkages present in both amylose and amylopectin. The single most striking observation was the loss of the C-6 resonance signal, indicating that the α-(1–6) glucosidic bonds associated with amylopectin branching were degraded entirely with the combined treatment, corroborating GPC results that showed amylopectin was inordinately degraded compared to amylose. Another notable change in NTS was the introduction of the resonance peaks assigned to the carbonyl carbon atom between δ 165 and 178 ppm, where a doublet at δ 170.28 and 168.44 ppm (*n.b.* aldehyde groups) plus peak shoulders at δ

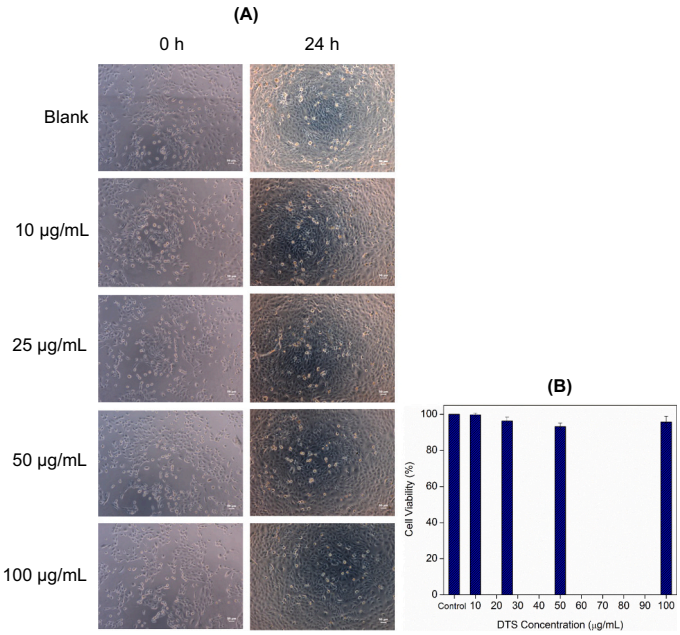

Fig. 6. Morphological changes (A) and viability (B) of HaCaT cells cultured in DTS solutions of various concentrations.

175.67 and 174.03 ppm (*n.b.* carboxyl groups) were observed. The carbonyl carbon signal provided evidence that NTS was oxidized. Similar results have also been reported by Yu et al. [66].

3.4. Thermal-degradation (decomposition) behaviour

The TG and the corresponding DTG profiles are presented in Fig. 4. It is apparent that TG weight-loss steps corresponded to DTG decomposition peaks. As can be seen from the DTG curve (Fig. 4(A)), NTS exhibited a two-step decomposition pattern. At the outset of the NTS curve, the weak peak had a DTG minimum at 71.03 °C with a weight-loss of 13.25%. The first degradation stage is associated with dehydration and loss of highly volatile components, and the subsequent stages, with thermal decomposition to produce CO_2, H_2O, and various hydrocarbon by-products [67]. It should be noted that decomposition under 300 °C is inextricably linked to water condensation from the inter- and intra-molecular OH groups of starch molecules [68]. Interestingly, NTS begins to decompose at *ca.* 300 °C [69]. Thus, due to decomposition, NTS had a relatively broad and strong peak centered at 384.54 °C, corresponding to 68.44% weight-loss and a small shoulder peak on the left-side at 346.03 °C. A comparable maximum degradation rate temperature (T_{max} ~ 384.54 °C) was previously reported [70]. In fact, an earlier study has shown that thermal decomposition results from the long-chain scission, particularly the α-1,4 linkages in amylose and amylopectin that are more susceptible to hydrolysis than α-1,6 linkages [70]. The authors have also reported that amylopectin-rich starches require more decomposition energy due to their high molecular weight and α-1,6 bonds. The residual char yield of NTS at 800 °C was 17.10%, indicating the possibility that much of the decomposition products were volatile. Subsequent to the combined treatment, DTS exhibited multiple weight-loss regions (Fig. 4(B)), ostensibly due to the sample's heterogeneity, which indicated thermal stability improvement. As described above, the first DTG peak at 93.79 °C with a weight-loss of 10.36% was assigned to loss of absorbed water from DTS. The DTG endotherm observed at 278.22 °C had a shoulder peak on the left-side at 240.25 °C, both with respective weight losses of 2.08 and 8.97% attributed to the loss of bounded water. As for the rest, the three endothermic peaks at 359.05, 559.75, and 667.15 °C and their corresponding weight losses of 1.53, 3.11, and 34.01% were ascribed to thermal decomposition of DTS, which involves cleavage of glycosidic linkages to produce various hydrocarbon and gaseous products. The first two DTG peaks at 359.05 and 559.75 °C were small and broad, and the one at 667.15 °C was sharper and taller compared to the other peaks. Thus, the T_{max} value was 667.15 °C, which was higher than that of NTS at *ca.* 384.54 °C, suggesting compact and more ordered crystalline structure as observed in PXRD results requiring more energy to degrade. The residual char amount of DTS was calculated as 39.31%, higher than NTS's, which was most likely due to improved thermal stability with the combined treatment, hence the reduced decomposition. Ayu et al. [71] and Fang et al. [72] pointed out that with fewer hydroxyl groups on the oxidized starches, decomposition decreases, synchronously improving thermal stability. Besides, high residual solids indicate the presence of non-volatile compounds at high levels.

3.5. Size and morphology

Photomicrographs detailing the morphological features and dimensions of NTS and DTS at 2500 x (A, B) and 5000 x (a, b) magnifications are given in Fig. 5. NTS granule sizes ranged from *approx.* 5 to 20-μm-diameter and were oval, truncated, and rounded. The truncated areas had flat, slightly undulated, convex, or concave surfaces (Fig. 5 (A)). Tukomane et al. [73] made similar observations and descriptions of the truncated areas of NTS granules. Granule surfaces were coarse-textured (Fig. 5(a)) with no discernible pores or fissures. The morphological appearance and diameter of NTS granules were as anticipated [74]. The combined treatment impact on morphology and size was apparent from the photomicrographs (Fig. 5(B, b)). Indeed, no intact granules were observed or measured. However, it is interesting and indeed remarkable that DTS had novel rod-like crystals and (or) structures with blunt or sharp ends and an average diameter and length of 393.55 nm and 5.22 μm, respectively. The observed morphological differences between NTS and DTS were attributed to the combined treatment. Thermal-acid hydrolysis and periodate oxidation of NTS led to the erosion and fracture of the amorphous and crystalline lamellae of granules, thereby allowing and, in many ways, facilitating the formation of rod-shaped DTS. In fact, it has been actually suggested that hydrolytic and oxidative cleavage of starch chains in the amorphous regions allows extensive re-ordering and packing of chain segments to yield a more crystalline structure [12]. More importantly, and as expected, iodine species removal indubitably allowed superior crystal packing and

Table 2
Ground state properties of NTS and DTS.

S·No	Coordinates	ZDO atomic charges	Mulliken atomic charges	ZDO atomic charges	Mulliken atomic charges
		DTS		NTS	
1	C	−0.2026	−0.3344	0.0328	−0.0179
2	C	−0.2101	−0.3428	−0.2170	−0.2459
3	C	−0.1236	−0.1937	0.1532	0.1451
4	C	−0.0182	−0.099	−0.0015	−0.0446
5	O	−0.2522	−0.2865	0.0450	0.0071
6	C	−0.2012	−0.3324	−0.0284	−0.0747
7	C	−0.209	−0.3412	−0.2117	−0.2448
8	C	−0.1311	−0.2011	−0.1106	−0.1272
9	C	−0.0218	−0.1	−0.3261	−0.3714
10	O	−0.2583	−0.2913	−0.3390	−0.3849
11	C	0.0005	−0.0427	−0.0185	−0.1032
12	O	−0.231	−0.2617	−0.3599	−0.4081
13	C	−0.0417	−0.1292	0.0270	−0.0247
14	C	−0.0504	−0.1322	−0.2561	−0.2873
15	C	0.1509	0.1286	0.1257	0.0989
16	C	0.0629	0.0227	0.0342	−0.0101
17	O	−0.3389	−0.3859	0.0443	−0.0004
18	C	−0.0145	−0.1015	−0.0330	−0.0811
19	O	−0.3857	−0.4355	−0.1396	−0.1605
20	O	−0.3878	−0.4378	−0.1201	−0.1367
21	H	0.0857	0.1375	−0.3730	−0.4216
22	H	0.0899	0.1441	−0.3574	−0.4046
23	H	0.0957	0.1516	−0.0122	−0.1015
24	H	0.0753	0.1211	−0.3893	−0.4397
25	H	0.0722	0.1174	0.0275	−0.0166
26	H	0.0901	0.1403	−0.2405	−0.2698
27	H	0.077	0.1235	0.1355	0.1157
28	H	0.0654	0.1092	0.0374	−0.0024
29	H	0.0813	0.1288	0.0325	−0.0079
30	H	0.0968	0.1526	−0.0039	−0.0431
31	H	0.0606	0.1047	−0.1251	−0.1450
32	H	0.0876	0.1422	−0.2180	−0.2500
33	H	0.0808	0.1281	−0.3578	−0.4048
34	H	0.0695	0.114	−0.3170	−0.3614
35	H	0.0873	0.1366	0.0239	−0.0598
36	H	0.0759	0.1221	−0.3736	−0.4227
37	H	0.0647	0.1084	−0.0685	−0.1881
38	H	0.0794	0.1263	−0.0822	−0.2086
39	H	0.0895	0.1435	0.0457	0.0879
40	H	0.0608	0.1036	0.0780	0.1314
41	H	0.0883	0.1421	0.1143	0.1782
42	H	0.1051	0.1615	0.0925	0.1503
43	H	0.0914	0.1433	0.0708	0.1234
44	H	0.0758	0.1256	0.0851	0.1374
45	H	0.0705	0.1144	0.1672	0.2400
46	H	0.2294	0.2643	0.0583	0.1044
47	H	0.1094	0.1685	0.0913	0.1469
48	H	0.0622	0.1079	0.2349	0.2702
49	H	0.2209	0.255	0.2117	0.2451
50	H	0.2253	0.2597	0.1036	0.1612

Note: ZDO = Zero-Differential Orbital; NTS = Native Tapioca Starch; DTS = Dialdehyde Tapioca Starch; C = Carbon; O = Oxygen; and H = Hydrogen.

forming of DTS, accordingly enhancing the rods morphology and homogeneity.

3.6. Color characteristics and changes

To ascertain how effective the removal of iodine species was, a white standard, NTS, iodine species-containing dialdehyde starch (DAS), and DTS, color measurements were taken and compared. Table 1 shows the results of the color parameters of the standard and the samples studied. Compared with the standard, NTS was white and had relatively low redness and yellowness positive values. The values fell within the ranges previously reported [75,76]. The luminosity (L^*) value reduced by *ca.* 26%, and DAS was thus darker than both the standard and NTS, indicating browning of the sample. According to Oriani et al. [77], the L^* parameter is an indicator of browning. DAS darkening behaviour can be explained by the fact that iodate ions undergo a reduction reaction to produce iodine molecules that darken over time [19,21]. The opposite was observed for DTS, which exhibited a higher L^* value than DAS and was, therefore, substantially white. The observed increase of the L^* parameter by *ca.* 30.02% indicated the removal of iodine species eliminated the browning effect, concomitantly increasing the whiteness aspect. As for the chromatic parameters, the a^* values of both DAS and DTS were greater than zero, indicating the presence of a red shade with DAS having a considerably higher value than that of DTS. DAS and DTS positive b^* values indicated that they both had a yellow tint. The high b^* and c^* positive values of DAS confirmed yellowing caused by iodine molecules and high color intensity, respectively. Besides, the low b^* and c^* positive values of DTS corroborated the effective removal of iodine species.

3.7. Cytotoxic effect and cell viability

The cytotoxicity of DTS is an important property for a wide range of biomaterial applications. No discernible abnormal morphology or cellular lysis was observed (Fig. 6(A)). However, few rounded and sparse HaCaT cells characteristic of inactive cells were present and increased with increasing DTS concentration. Low M_w substances diffuse into cells and react with the inside components resulting in cell death [43]. No cytotoxicity effect could be determined from the blank control over the test period. As for DTS, the cell viability of the 10 μg/mL concentration (Fig. 6(B)) was slightly lower than that of the control but was the highest compared to the other concentrations, meaning, though not significant, higher DTS amounts reduced viability. The moderate decrease in viability from 99.71% (10 μg/mL) to 96.26% (25 μg/mL) and 93.31% (50 μg/mL) was a difference of *ca.* 3% between two successive concentrations. Interestingly, a slight increase in viability from 93.31% (50 μg/mL) to 95.75% (100 μg/mL) was noted on doubling DTS concentration. Generally, comparing the control's cell viability and those of the other concentrations and especially the least at 93.31% (50 μg/mL), indicated that DTS had no significant cytotoxicity on HaCaT cells. Besides, at low concentrations, particularly 10 μg/mL, DTS exhibited excellent cellular compatibility, as it almost did not alter cell viability. The low DTS cytotoxicity is ascribable to its relatively high M_w (~57.81 kDa), which is large enough to inhibit it from diffusing into cells [43]. Overall, DTS can, therefore, be used for biomaterial applications.

3.8. Conformations and structural features

Table 2 contains computed values of the bond order between atoms (coordinates) in NTS and DTS. Geometry optimization was achieved for NTS and DTS (Fig. 7(A and C)) confined structures after a projection of *approx.* 10,000 iterations. Convergence was recorded at 10^{-10} kcal/mol. The maximum number of self-consistent field (SCF) iteration calculations were performed until NTS and DTS structures converged and yielded final SCF energies, NTS = −184.9 au and DTS = −151.7 au. The x, y, z ground state dipole coordinates of DTS were 1.3527 (x), 1.0073 (y), and 2.5947 (z), and a dipole moment of 3.09 D. The measured zero-differential orbital (ZDO) and Mulliken atomic charges summarized in Table 2 spell-out the atomic coordinates of NTS and DTS with measured respective heat formation energies of *ca.* −543.7 and −289 kcal/mol. A less positive energy indicates a relatively stable and less reactive compound. The SCF converged NTS and DTS are presented in Fig. 7(B and D).

The structure of the compounds, frontier orbitals (*i.e.,* HOMO and LUMO), and molecular orbital numbers of NTS and DTS are shown in Fig. 8(A-D). The HOMO (DTS) acts as a non-bonding type that is in the plane of NTS (Fig. 8(A)) and DTS (Fig. 8(B)), whilst the LUMO is a π orbital perpendicular in p_z orbital to the NTS molecule plane. The first excited state of DTS is an n → π* transition composed almost exclusively of the HOMO→LUMO transition, which is the lowest energy transition in the ground state. Reactions occur in the frontier molecular orbitals as

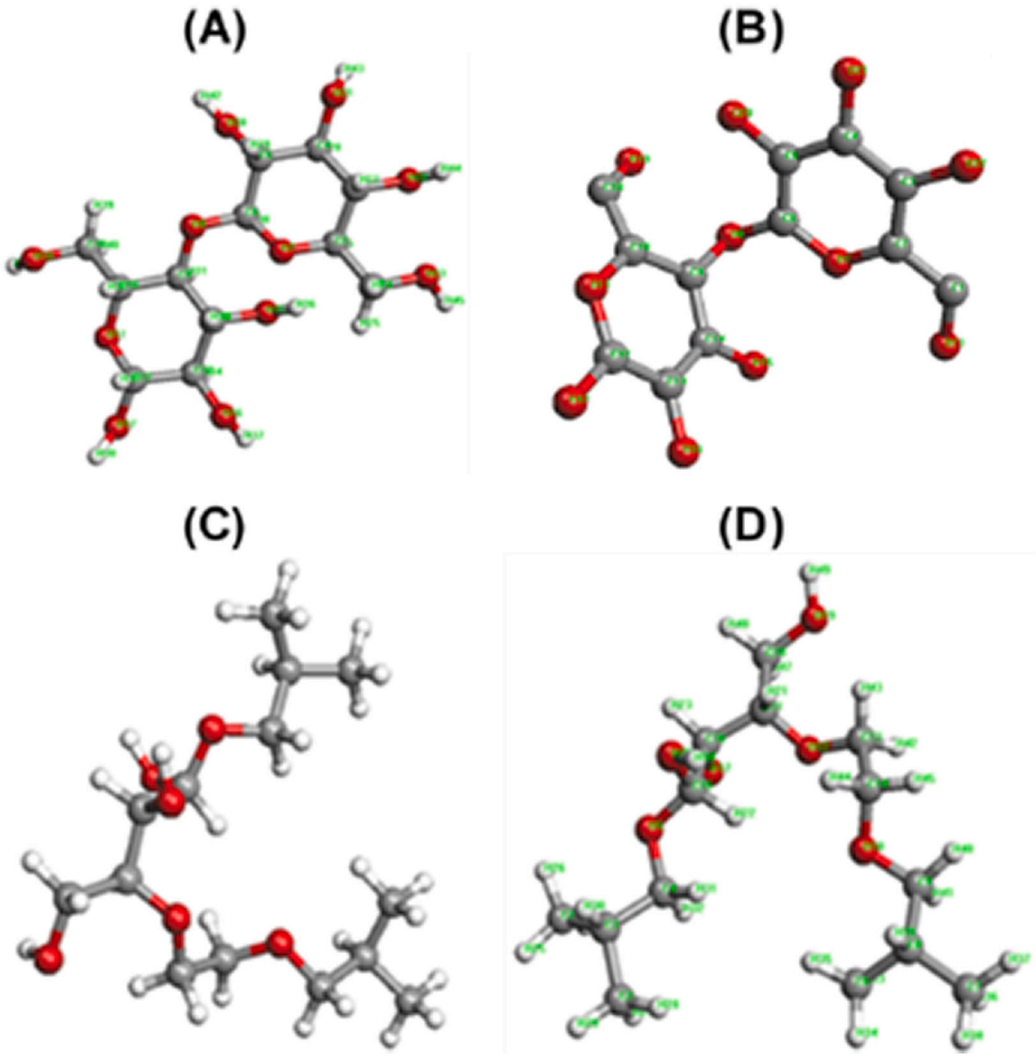

Fig. 7. Structural alignment of NTS (A) and DTS (C), and SCF Converged NTS (B) and DTS (D).

the electrons in the HOMO have the most energy, and LUMO is the most probable and energetically favorable location for a bond to occur. A mapped surface has the isosurface contoured and color-coded by data from Grid 1 and 2, respectively [78]. The mapped surface density difference between NTS (Fig. 8(C)) and DTS (Fig. 8(D)) can be observed in the electrostatic potential (ESP) density surfaces of the ground-state electron density.

ESP surface measurements of NTS (Fig. 9(A)) and DTS (Fig. 9(B)) were obtained to establish and demonstrate the movement of electrons in the excitation state. NTS and DTS surfaces showed the shift of electron density from in-plane near the oxygen to out-of-the-plane near the carbon. The blue end shows where ESP increased, which indicates and confirms that the NTS and DTS domains' electron density decreased. A decrease in the electron density along the NTS and DTS backbone means the interaction energy with the positive test charge becomes less negative or increases, bringing about the blue color. The red regions indicate ESP decreased (*i.e.,* become more negative) since the region's electron density increased. In Fig. 9(C) and (D), the solvent accessible surfaces were calculated to evaluate NTS and DTS areas available for the water molecule interaction. Using the self-consistent reaction field (SCRF) approach, solvation was carried out in the water with a dielectric constant of 78.3 and 1.33 refractive index. Aqueous treatment of the confined reactive functional groups makes it possible and much easier for other biomolecules or proteins to interact with the DTS molecule.

4. Conclusions

In summary, the combined treatment produced DTS with little or no iodine species and markedly high percent yield, aldehyde content, and water-solubility. By studying and comparing the M_w, structural-spectral, thermal, morphological, color, cell viability, and conformational properties of NTS and DTS, it was found that the combined treatment, first, significantly reduced the M_w and granular size. Secondly, it induced a transformation of polymorphs of NTS and elevated crystallinity and heat-stability. Thirdly, augmented surface homogeneity, and color. Fourthly, DTS had a low cytotoxic effect at the concentrations assayed. Lastly, DTS was more chemically reactive than NTS, as substantiated by the conformational energies (*i.e.,* SCF energy and heat formation energy) and HOMO→LUMO transition. Most importantly, no adverse effects on the various properties were observed. One can, therefore, envisage interesting potential applications in biomaterial, medical and food industries.

CRediT authorship contribution statement

Peter N. Kariuki: Conceptualization, Methodology, Investigation, Formal analysis, Validation, Data curation, Software, Writing - original draft preparation. **Yasothai Arjunan:** Methodology, Investigation, Formal analysis. **Usharani Nagarajan:** Conceptualization, Methodology, Validation, Writing - review & editing. **Swarna V. Kanth:**

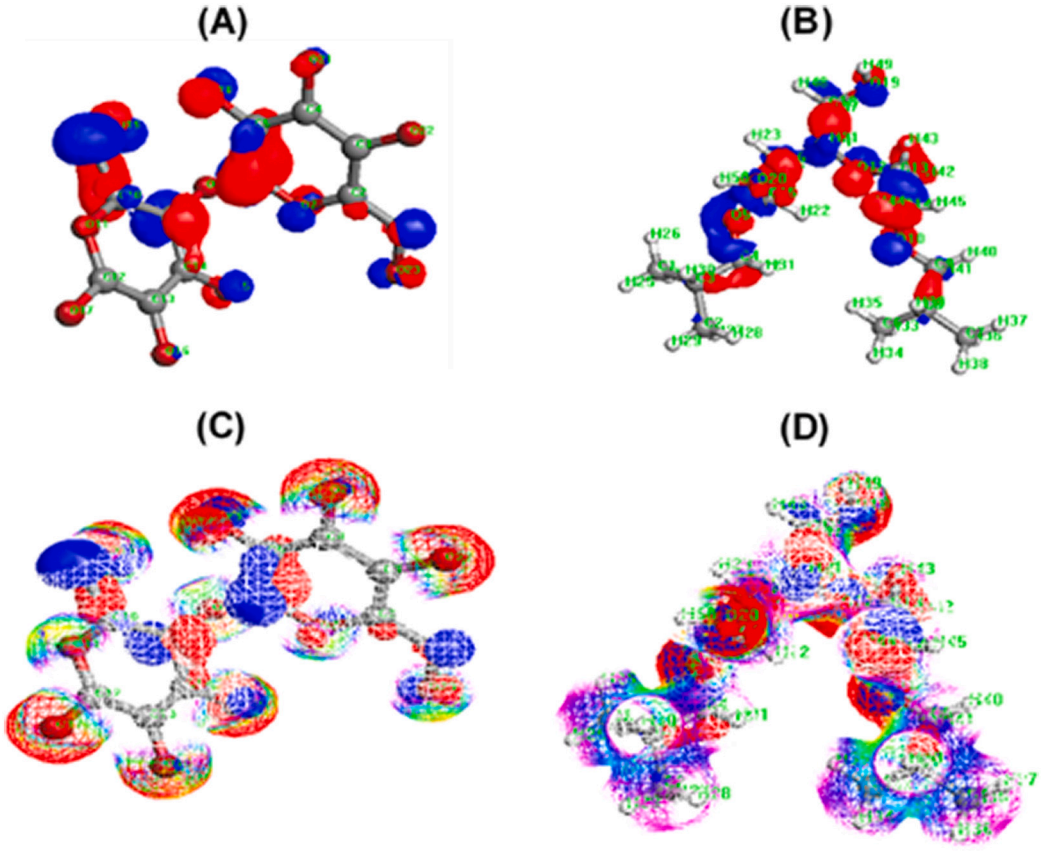

Fig. 8. Mapped surfaces in the molecular orbital arrangement of NTS (A) and DTS (B) and ESP density surfaces of NTS (C) and DTS (D).

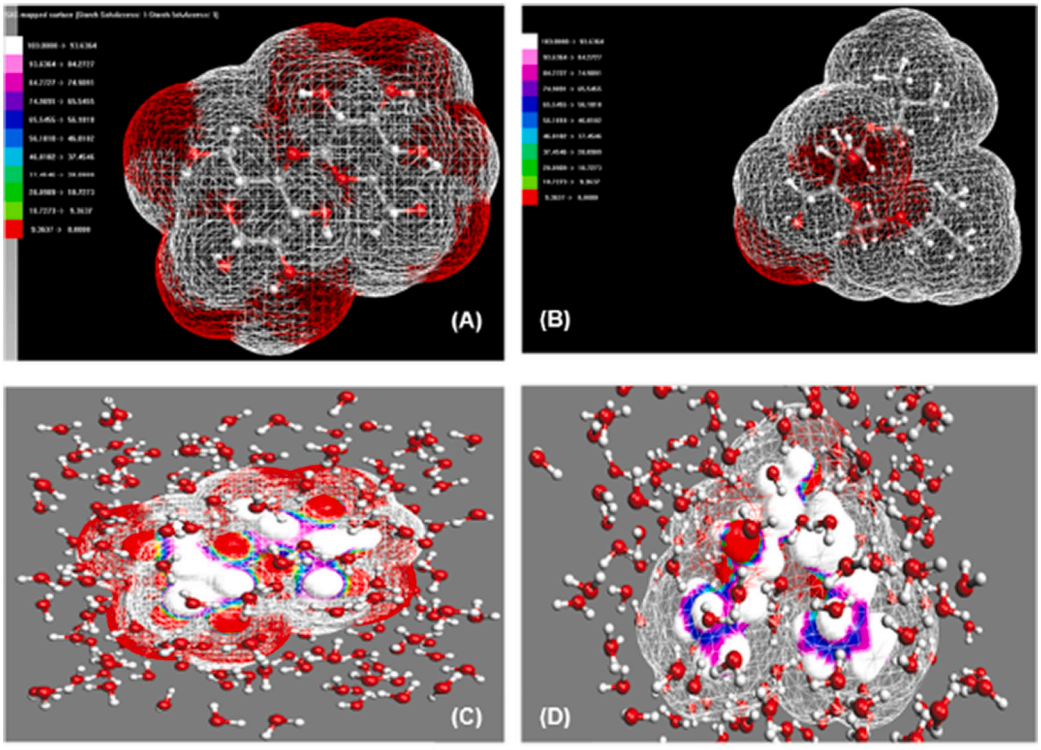

Fig. 9. ESP surface measurements of NTS (A) and DTS (B) and solvent accessible surfaces of NTS (C) and DTS (D).

Conceptualization, Supervision, Resources, Project administration, Funding acquisition.

Declaration of competing interest

Authors declare no conflict of interest.

Acknowledgments

Peter N. Kariuki gratefully acknowledges the financial support provided by the Dedan Kimathi University of Technology (Nyeri, Kenya), and appreciates the technical support from the Department of Leather Technology (Housed at CSIR-Central Leather Research Institute (CLRI)), Alagappa College of Technology, Anna University (Chennai, India). Authors thank CATERS, CSIR-CLRI (Chennai, India) for their support in testing and characterization and acknowledge the funding support from CSIR-Integrated Skill Initiative Program (India) - NWP-0100 (CSIR-CLRI Communication No. 1406).

References

[1] D.W. Gade, Names for Manihot esculenta: geographical variation and lexical clarification, J. Lat. Am. Geogr. 1 (2003) 43–57.
[2] H. Ceballos, R.S. Kawuki, V.E. Gracen, G.C. Yencho, C.H. Hershey, Conventional breeding, marker-assisted selection, genomic selection and inbreeding in clonally propagated crops: a case study for cassava, Theor. Appl. Genet. 128 (2015) 1647–1667.
[3] P.V.F. Lemos, L.S. Barbosa, I.G. Ramos, R.E. Coelho, J.I. Druzian, Characterization of amylose and amylopectin fractions separated from potato, banana, corn, and cassava starches, Int. J. Biol. Macromol. 132 (2019) 32–42.
[4] A. Verma, A. Gaur, V.K. Singh, Mechanical properties and microstructure of starch and sisal fiber biocomposite modified with epoxy resin, Mater. Perform. Charact. 6 (2017) 500–520.
[5] R. Wongsagonsup, P. Deeyai, W. Chaiwat, S. Horrungsiwat, K. Leejariensuk, M. F. Suphantharika, A. Uongfuchat, S. Dangtip, Modification of tapioca starch by non-chemical route using jet atmospheric argon plasma, Carbohydr. Polym. 102 (2014) 790–798.
[6] B.C. Maniglia, D.C. Lima, M.D. Matta Junior, P. Le-Bail, A. Le-Bail, P.E.D. Augusto, Hydrogels based on ozonated cassava starch: effect of ozone processing and gelatinization conditions on enhancing 3D-printing applications, Int. J. Biol. Macromol. 138 (2019) 1087–1097.
[7] J. Xing, Y. Liu, D. Li, L. Wang, B. Adhikari, Heat-moisture treatment and acid hydrolysis of corn starch in different sequences, LWT - Food Sci. Technol. 79 (2017) 11–20.
[8] D. Lund, K.J. Lorenz, Influence of time, temperature, moisture, ingredients, and processing conditions on starch gelatinization, Crit.Rev. Food Sci. Nutr. 20 (1984) 249–273.
[9] J. Lelievre, H. Liu, A review of thermal analysis studies of starch gelatinization, Thermochim. Acta 246 (1994) 309–315.
[10] S. Wang, L. Copeland, Molecular disassembly of starch granules during gelatinization and its effect on starch digestibility: a review, Food Funct. 4 (2013) 1564–1580.
[11] S. Wang, C. Li, L. Copeland, Q. Niu, S. Wang, Starch retrogradation: a comprehensive review, Compr. Rev. Food Sci. Food Saf. 14 (2015) 568–585.
[12] S. Wang, L. Copeland, Effect of acid hydrolysis on starch structure and functionality: a review, Crit. Rev. Food Sci. Nutr. 55 (2015) 1081–1097.
[13] M. Pratiwi, D.N. Faridah, H.N. Lioe, Structural changes to starch after acid hydrolysis, debranching, autoclaving-cooling cycles, and heat moisture treatment (HMT): a review, Starch 70 (2018) 1700028.
[14] R. Hoover, Acid-treated starches, Food Rev. Int. 16 (2000) 369–392.
[15] N.L. Vanier, S.L.M. El Halal, A.R.G. Dias, E. da Rosa Zavareze, Molecular structure, functionality and applications of oxidized starches: a review, Food Chem. 221 (2017) 1546–1559.
[16] J.W. Sloan, B.T. HoFreiter, R.L. Mellies, I.A. Wolff, Properties of periodate oxidized starch, Ind. Eng. Chem. 48 (1956) 1165–1172.
[17] K.A. Kristiansen, A. Potthast, B.E. Christensen, Periodate oxidation of polysaccharides for modification of chemical and physical properties, Carbohydr. Res. 345 (2010) 1264–1271.
[18] R.D. Guthrie, in: The “dialdehydes” from the periodate oxidation of carbohydrates, 1962, pp. 105–158.
[19] P.N. Kariuki, A. Yasothai, G.C. Jayakumar, S.V. Kanth, A pragmatic approach towards the manufacture of wet-white leathers using a bio-polymeric tanning system, in: 35th IULTCS Congr. 2019 "Benign by Des. Leather - Futur. Through Sci. Technol., International Union of Leather Technologists and Chemists Societies, Dresden-Germany, 2019, pp. 1–5.
[20] R. Wongsagon, S. Shobsngob, S. Varavinit, Preparation and physicochemical properties of dialdehyde tapioca starch, Starch 57 (2005) 166–172.
[21] A. Gennadios, A. Handa, G.W. Froning, C.L. Weller, M.A. Hanna, Physical properties of egg white-dialdehyde starch films, J. Agric. Food Chem. 46 (1998) 1297–1302.
[22] R.N. Waduge, S. Xu, K. Seetharaman, Iodine absorption properties and its effect on the crystallinity of developing wheat starch granules, Carbohydr. Polym. 82 (2010) 786–794.
[23] J.M. Bobbitt, Periodate oxidation of carbohydrates, in: M.L. Wolfrom (Ed.), Adv. Carbohydr. Chem, 11th ed., Academic Press Inc., New York, 1956, pp. 1–41.
[24] W. Ding, Y.N. Wang, J.F. Zhou, B. Shi, Effect of structure features of polysaccharides on properties of dialdehyde polysaccharide tanning agent, Carbohydr. Polym. 201 (2018) 549–556.
[25] X. Yang, Y. Chen, S. Yao, J. Qian, H. Guo, X. Cai, Preparation of immobilized lipase on magnetic nanoparticles dialdehyde starch, Carbohydr. Polym. 218 (2019) 324–332.
[26] S. Xiao, X. Liu, C. Tong, L. Zhao, X. Liu, A. Zhou, Y. Cao, Dialdehyde starch nanoparticles as antitumor drug delivery system: an in vitro, in vivo, and immunohistological evaluation, Chin. Sci. Bull. 57 (2012) 3226–3232.
[27] A. Naz, K. Bano, F. Bano, N.A. Ghafoor, N. Akhtar, Conformational analysis (geometry optimization) of nucleosidic antitumor antibiotic showdomycin by ArgusLab 4 software, Pak. J. Pharm. Sci. 22 (2009) 78–82.
[28] C. Hernández-Jaimes, R.G. Utrilla-Coello, H. Carrillo-Navas, E. García-Márquez, M. Meraz, L.A. Bello-Pérez, E.J. Vernon-Carter, J. Alvarez-Ramirez, Corn starch acid hydrolysis at the onset gelatinization temperature: morphology, crystallinity, viscoelasticity, and thermal properties, Starch 66 (2014) 636–644.
[29] S.V. Kanth, A. Ramaraj, J.R. Rao, B.U. Nair, Stabilization of type I collagen using dialdehyde cellulose, Process Biochem. 44 (2009) 869–874.
[30] K. Babor, V. Kaláč, K. Tihlárik, Periodate oxidation of saccharides. III. Comparison of the methods for determining the consumption of sodium periodate and the amount of formic acid formed, Chem. Pap. 27 (1973) 676–680.
[31] M. Vithanage, I. Herath, S.S. Achinthya, T. Bandara, L. Weerasundara, S. S. Mayakaduwa, Y. Jayawardhana, P. Kumarathilaka, Iodine in commercial edible iodized salts and assessment of iodine exposure in Sri Lanka, Arch. Public Health 74 (2016) 21.
[32] M.O. Adedokun, O.A. Itiola, Material properties and compaction characteristics of natural and pregelatinized forms of four starches, Carbohydr. Polym. 79 (2010) 818–824.
[33] D.B. Cruz, W.S.V. Silva, I.P. Santos, E.S. Zavareze, M.C. Elias, Structural and technological characteristics of starch isolated from sorghum as a function of drying temperature and storage time, Carbohydr. Polym. 133 (2015) 46–51.
[34] C.K. Ozkan, H. Ozgunay, H. Akat, Possible use of corn starch as tanning agent in leather industry: controlled (gradual) degradation by H2O2, Int. J. Biol. Macromol. 122 (2019) 610–618.
[35] B.T. Hofreiter, B.H. Alexander, I.A. Wolff, Rapid estimation of dialdehyde content of periodate oxystarch through quantitative alkali consumption, Anal. Chem. 27 (1955) 1930–1931.
[36] M. Fiedorowicz, A. Para, Structural and molecular properties of dialdehyde starch, Carbohydr. Polym. 63 (2006) 360–366.
[37] L. Zhang, W. Xie, X. Zhao, Y. Liu, W. Gao, Study on the morphology, crystalline structure and thermal properties of yellow ginger starch acetates with different degrees of substitution, Thermochim. Acta 495 (2009) 57–62.
[38] N. Atichokudomchai, S. Varavinit, P. Chinachoti, A study of ordered structure in acid-modified tapioca starch by 13C CP/MAS solid-state NMR, Carbohydr. Polym. 58 (2004) 383–389.
[39] C. Mutungi, L. Passauer, C. Onyango, D. Jaros, H. Rohm, Debranched cassava starch crystallinity determination by Raman spectroscopy: correlation of features in Raman spectra with X-ray diffraction and 13C CP/MAS NMR spectroscopy, Carbohydr. Polym. 87 (2012) 598–606.
[40] Y. Zuo, W. Liu, J. Xiao, X. Zhao, Y. Zhu, Y. Wu, Preparation and characterization of dialdehyde starch by one-step acid hydrolysis and oxidation, Int. J. Biol. Macromol. 103 (2017) 1257–1264.
[41] N. Atichokudomchai, S. Shobsngob, S. Varavinit, Morphological properties of acid-modified tapioca starch, Starch 52 (2000) 283–289.
[42] G.K. Priya, M.M.A. Javid, A. George, M. Aarthy, A.S. Durai, N.R. Kamini, M. K. Gowthaman, R. Aravindhan, S. Ganesh, R. Chandrasekar, N. Ayyadurai, Next generation greener leather dyeing process through recombinant green fluorescent protein, J. Clean. Prod. 126 (2016) 698–706.
[43] X. Wang, Z. Gu, H. Qin, L. Li, X. Yang, X. Yu, Crosslinking effect of dialdehyde starch (DAS) on decellularized porcine aortas for tissue engineering, Int. J. Biol. Macromol. 79 (2015) 813–821.
[44] M.A. Thompson, QM/MMpol: a consistent model for solute/solvent polarization. Application to the aqueous solvation and spectroscopy of formaldehyde, acetaldehyde, and acetone, J. Phys. Chem. 100 (1996) 14492–14507.
[45] M.J.S. Dewar, E.G. Zoebisch, E.F. Healy, J.J.P. Stewart, Development and use of quantum mechanical molecular models. 76. AM1: a new general purpose quantum mechanical molecular model, J. Am. Chem. Soc. 107 (1985) 3902–3909.
[46] H.A.M. Wickramasinghe, S. Takigawa, C. Matsuura-Endo, H. Yamauchi, T. Noda, Comparative analysis of starch properties of different root and tuber crops of Sri Lanka, Food Chem. 112 (2009) 98–103.
[47] J.N. BeMiller, K.C. Huber, Starch, in: R. Daniel, R.L. Whistler, H. Roeper (Eds.), Ullmann's Encycl. Ind. Chem, 7th ed., Wiley-VCH Verlag GmbH & Co. KGaA, Weinheim, Germany, 2011, pp. 1–28.
[48] V. Horváth, I.R. Epstein, K. Kustin, Mechanism of the ferrocyanide-iodate-sulfite oscillatory chemical reaction, J. Phys. Chem. A 120 (2016) 1951–1960.
[49] L. Xu, A.K. Horvath, A possible candidate to be classified as an autocatalysis-driven clock reaction: kinetics of the pentathionate-iodate reaction, J. Phys. Chem. A 118 (2014) 6171–6180.
[50] C.M.L. Franco, C. Ogawa, T. Rabachini, T.S. Rocha, M.P. Cereda, J. Jane, Effect of lactic acid and UV irradiation on the cassava and corn starches, Braz. Arch.Biol. Technol. 53 (2010) 443–454.

[51] H. Xia, B.-Z. Li, Q. Gao, Effect of molecular weight of starch on the properties of cassava starch microspheres prepared in aqueous two-phase system, Carbohydr. Polym. 177 (2017) 334–340.
[52] J. Huang, Z. Shang, J. Man, Q. Liu, C. Zhu, C. Wei, Comparison of molecular structures and functional properties of high-amylose starches from rice transgenic line and commercial maize, Food Hydrocoll. 46 (2015) 172–179.
[53] N. Atichokudomchai, S. Varavinit, P. Chinachoti, Gelatinization transitions of acid-modified tapioca starches by Differential Scanning Calorimetry (DSC), Starch 54 (2002) 296–302.
[54] E. de M. Teixeira, A.A.S. Curvelo, A.C. Corrêa, J.M. Marconcini, G.M. Glenn, L.H. C. Mattoso, Properties of thermoplastic starch from cassava bagasse and cassava starch and their blends with poly (lactic acid), Ind. Crops Prod. 37 (2012) 61–68.
[55] M.C. Garcia, C.M.L. Franco, M.S.S. Júnior, M. Caliari, Structural characteristics and gelatinization properties of sour cassava starch, J. Therm. Anal. Calorim. 123 (2016) 919–926.
[56] Y. Li, C. Li, Z. Gu, Y. Hong, L. Cheng, Z. Li, Effect of modification with 1,4-α-glucan branching enzyme on the rheological properties of cassava starch, Int. J. Biol. Macromol. 103 (2017) 630–639.
[57] A. Agi, R. Junin, A. Gbadamosi, A. Abbas, N.B. Azli, J. Oseh, Influence of nanoprecipitation on crystalline starch nanoparticle formed by ultrasonic assisted weak-acid hydrolysis of cassava starch and the rheology of their solutions, Chem. Eng. Process. 142 (2019), 107556.
[58] Y.I. Cornejo-Ramírez, O. Martínez-Cruz, C.L. Del Toro-Sánchez, F.J. Wong-Corral, J. Borboa-Flores, F.J. Cinco-Moroyoqui, The structural characteristics of starches and their functional properties, CyTA - J. Food. 16 (2018) 1003–1017.
[59] L.M.K. Ferrini, T.S. Rocha, I.M. Demiate, C.M.L. Franco, Effect of acid-methanol treatment on the physicochemical and structural characteristics of cassava and maize starches, Starch 60 (2008) 417–425.
[60] C. Mutungi, S. Schuldt, C. Onyango, Y. Schneider, D. Jaros, H. Rohm, Dynamic moisture sorption characteristics of enzyme-resistant recrystallized cassava starch, Biomacromolecules 12 (2011) 660–671.
[61] S. Khatoon, Y.N. Sreerma, D. Raghavendra, S. Bhattacharya, K.K. Bhat, Properties of enzyme modified corn, rice and tapioca starches, Food Res. Int. 42 (2009) 1426–1433.
[62] V. Singh, S.Z. Ali, S. Divakar, 13C CP/MAS NMR spectroscopy of native and acid modified starches, Starch 45 (1993) 59–62.
[63] F. Horii, H. Yamamoto, A. Hirai, R. Kitamaru, Structural study of amylose polymorphs by cross-polarization-magic-angle spinning, 13C-NMR spectroscopy, Carbohydr. Res. 160 (1987) 29–40.
[64] A. Flores-Morales, M. Jiménez-Estrada, R. Mora-Escobedo, Determination of the structural changes by FT-IR, Raman, and CP/MAS 13C NMR spectroscopy on retrograded starch of maize tortillas, Carbohydr. Polym. 87 (2012) 61–68.
[65] M.J. Gidley, Quantification of the structural features of starch polysaccharides by N.M.R. spectroscopy, Carbohydr. Res. 139 (1985) 85–93.
[66] Y. Yu, Y. Wang, W. Ding, J. Zhou, B. Shi, Preparation of highly-oxidized starch using hydrogen peroxide and its application as a novel ligand for zirconium tanning of leather, Carbohydr. Polym. 174 (2017) 823–829.
[67] X. Liu, L. Yu, F. Xie, M. Li, L. Chen, X. Li, Kinetics and mechanism of thermal decomposition of cornstarches with different amylose/amylopectin ratios, Starch 62 (2010) 139–146.
[68] W. Thitisomboon, P. Opaprakasit, N. Jaikaew, S. Boonyarattanakalin, Characterizations of modified cassava starch with long chain fatty acid chlorides obtained from esterification under low reaction temperature and its PLA blending, J. Macromol. Sci. A 55 (2018) 253–259.
[69] N.E. Wahyuningtiyas, H. Suryanto, E. Rudiyanto, S. Sukarni, P. Puspitasari, Thermogravimetric and kinetic analysis of cassava starch based bioplastic, J. Mech. Eng. Sci. Technol. 1 (2017) 69–77.
[70] A.F.K. Minakawa, P.C.S. Faria-Tischer, S. Mali, Simple ultrasound method to obtain starch micro- and nanoparticles from cassava, corn and yam starches, Food Chem. 283 (2019) 11–18.
[71] R.S. Ayu, A. Khalina, A.S. Harmaen, K. Zaman, M. Jawaid, C.H. Lee, Effect of modified tapioca starch on mechanical, thermal, and morphological properties of PBS blends for food packaging, Polymers (Basel) 10 (2018) 1187.
[72] J.M. Fang, P.A. Fowler, J. Tomkinson, C.A.S. Hill, The preparation and characterisation of a series of chemically modified potato starches, Carbohydr. Polym. 47 (2002) 245–252.
[73] T. Tukomane, P. Leerapongnum, S. Shobsngob, S. Varavinit, Preparation and characterization of annealed enzymatically hydrolyzed tapioca starch and utilization in tableting, Starch 59 (2007) 33–45.
[74] F. Zhu, Composition, structure, physicochemical properties, and modifications of cassava starch, Carbohydr. Polym. 122 (2015) 456–480.
[75] O. Ayetigbo, S. Latif, A. Abass, J. Müller, Comparing characteristics of root, flour and starch of biofortified yellow-flesh and white-flesh cassava variants, and sustainability considerations: a review, Sustainability 10 (2018) 1–32.
[76] M.M.P. Andrade, C.S. Oliveira, T.A.D. Colman, F.J.O.G. Costa, E. Schnitzler, Effects of heat–moisture treatment on organic cassava starch, J. Therm. Anal. Calorim. 115 (2014) 2115–2122.
[77] V.B. Oriani, G. Molina, M. Chiumarelli, G.M. Pastore, M.D. Hubinger, Properties of cassava starch-based edible coating containing essential oils, J. Food Sci. 79 (2014) E189–E194.
[78] I.E. Otuokere, F.J. Amaku, Conformation analysis and self-consistent field energy of immune response modifier, 1-(2-methylpropyl)-1H-imidazo[4,5]quinolin-4-amine (Imiquimod), Asian J. Res. Pharm. Sci. 5 (2015) 175.